Single-particle structure of silicon isotopes approaching ^{42}Si

S. R. Stroberg, A. Gade, J. A. Tostevin, V. M. Bader, T. Baugher, D. Bazin, J. S. Berryman, B. A. Brown, C. M. Campbell, K. W. Kemper, C. Langer, E. Lunderberg, A. Lemasson, S. Noji, F. Recchia, C. Walz, D. Weisshaar, and S. J. Williams

Phys. Rev. C **90**, 034301 — Published 3 September 2014

DOI: 10.1103/PhysRevC.90.034301

Single-particle structure of silicon isotopes approaching ^{42}Si

S.R. Stroberg,[1,2] A. Gade,[1,2] J.A. Tostevin,[3] V.M. Bader,[1,2] T. Baugher,[1,2] D. Bazin,[1,2] J.S. Berryman,[1] B.A. Brown,[1,2] C.M. Campbell,[4] K.W. Kemper,[5] C. Langer,[1,6] E. Lunderberg,[1,2] A. Lemasson,[1] S. Noji,[1] F. Recchia,[1] C. Walz,[1] D. Weisshaar,[1] and S.J. Williams[1]

[1] *National Superconducting Cyclotron Laboratory, Michigan State University, East Lansing, Michigan 48824, USA*
[2] *Department of Physics and Astronomy, Michigan State University, East Lansing, Michigan 48824, USA*
[3] *Faculty of Engineering and Physical Sciences, University of Surrey, Guildford, Surrey, GU2 7XH, United Kingdom*
[4] *Lawrence Berkeley National Laboratory, Berkeley, California 94720, USA*
[5] *Department of Physics, Florida State University, Tallahassee, Florida 32306, USA*
[6] *Joint Institute for Nuclear Astrophysics, Michigan State University, East Lansing, MI 48824, USA*

The structure of the neutron-rich silicon isotopes ^{36,38,40}Si was studied by one-neutron and one-proton knockout reactions at intermediate beam energies. We construct level schemes for the knockout residues ^{35,37,39}Si and ^{35,37,39}Al and compare knockout cross sections to the predictions of an eikonal model in conjunction with large-scale shell model calculations. The agreement of these calculations with the present experiment lends support to the microscopic explanation of the enhanced collectivity in the region of ^{42}Si. We also present an empirical method for reproducing the observed low-momentum tails in the parallel momentum distributions of knockout residues.

PACS numbers: 21.10.-k, 21.10.Pc, 23.20.Lv,21.60.Cs, 24.10.Ht, 24.50.+g, 29.30.Kv

I. INTRODUCTION

In nuclear physics the concept of shell closures – or magic numbers – underpins the predictive power of the nuclear shell model, reducing the necessary degrees of freedom and allowing nuclear properties to be understood in terms of a few valence nucleons outside of an inert core. Understanding how shell closures arise and how they evolve across the nuclear chart is therefore crucial to predicting nuclear properties. A particularly interesting case is that of the N=28 shell gap, the first shell gap which is not predicted by a simple harmonic oscillator potential, but which requires a strongly attractive spin-orbit component of the mean field potential. In addition, recent calculations suggest that three nucleon forces are required to generate this shell gap with a realistic nuclear interaction [1] .

Early suggestions of a disappearance of the N=28 gap at large isospin came from the low-lying 2_1^+ energy and enhanced $E2$ transition strength in ^{44}S [2]. However, the question remained whether this enhanced collectivity was due mostly to protons, which do not have a closed shell configuration at $Z = 16$ [3]. The measurement of a low-lying 2_1^+ energy [4] and the suggestion of a rotational $E(4_1^+)/E(2_1^+)$ ratio [5] at ^{42}Si, which has a nominal Z=14 sub-shell closure, made a strong case that N=28 is no longer a good shell closure in that region.

The microscopic explanation for the collapse of the $N = 28$ shell gap, as given in [4, 7], is the following. The filling of the neutron $0f_{7/2}$ orbit, due to the effect of the tensor force [8, 9], reduces the $Z = 14$ gap relative to ^{34}Si. Likewise, the removal of protons from the $0d_{3/2}$ orbit reduces the $N = 28$ gap relative to ^{48}Ca [6], due to the tensor force, and possibly the two-body spin-orbit force [10]. Excitations across the shrunken $Z = 14$ and $N = 28$ gaps are of a quadrupole nature and mutually enhance one another, leading to deformation, as discussed within the context of SU(3) symmetries [11] or a nuclear Jahn-Teller effect [7].

Thus far, experimental investigations into the region around ^{42}Si have generally employed collective observables, leaving some ambiguity as to the underlying single-particle picture of the shell gap evolution. In this work, we investigate the single-particle structure of ^{36,38,40}Si, along the isotopic chain connecting ^{34}Si, which exhibits closed-shell properties, to ^{42}Si, via one-proton and one-neutron knockout reactions. These reactions probe single-particle degrees of freedom, and are sensitive to the occupations of orbitals near the Fermi surface. We may therefore test whether the trend in single-particle degrees of freedom also reflects the proposed influence of the tensor force and mutual enhancement of collectivity.

This paper is organized as follows: In Section II we will describe the experimental setup and analysis. In Section III we outline the theoretical framework used in the analysis of this experiment. In Section IV we detail the level schemes we have constructed for the knockout residues, which allow us to assign partial cross sections to individual final states in the residue. In Section V we give the resulting inclusive and partial knockout cross sections and discuss their implications for the structure of the silicon isotopic chain. Finally, in Section VI we describe the empirical method used to obtain asymmetric momentum distributions from the symmetric calculated distributions.

II. EXPERIMENT

The experiment was performed at the Coupled Cyclotron Facility at the National Superconducting Cyclotron Laboratory at Michigan State University. Secondary beams of ^{36,38,40}Si were produced by fragmen-

tation of a 140 MeV/u ^{48}Ca primary beam interacting with a ^{9}Be production target, and purified in the A1900 fragment separator [13] before being delivered to the experimental station. Specifics of the secondary beams are given in Table I.

The secondary beams were then impinged on a ^{9}Be reaction target located in front of the S800 spectrograph [14]. The heavy reaction residues were identified on an event-by-event basis by an ionization chamber in the focal plane of the S800 spectrograph and plastic scintillators in the beam line for time-of-flight information. The position and angle of the residues were measured using two cathode-readout drift chambers, and the trajectory of the particle was traced back to the target using the ion optics code COSY [15], yielding the momentum vector and non-dispersive position at the target.

Prompt γ-rays were detected with the GRETINA array [16], surrounding the target position of the S800. Doppler-reconstruction was performed on an event-by-event basis, with the highest-energy interaction from GRETINA's online decomposition taken to be the first hit and used to reconstruct the angle of emission assuming the decay happened at the center of the target. All interactions within a single crystal were assumed to originate from the same γ-ray. For peak-identification, an add-back procedure was performed in which all adjacent crystals with interactions were combined. The add-back procedure was not used to obtain absolute peak intensities. The uncertainties in γ-ray peak energies are dominated by uncertainties in the Doppler reconstruction.

Gamma-ray intensities were obtained by a maximum likelihood fit of the measured spectrum with a sum of simulated detector response functions produced with the Geant4 simulation package [17]. The simulation was based on the AGATA simulation [18], modified to the GRETINA geometry and fine-tuned to reproduce the absolute efficiency measured with calibration sources. The simulation also accounted for effects of the Lorentz boost from the projectile frame to the lab frame. In addition to discrete γ rays emitted in flight by the reaction residue, rest-frame lines from positron annihilation and neutron-induced reactions in germanium and the aluminum beam pipe were simulated, as well as a continuous exponential background, which is described in more detail in Section VI. Detector thresholds were modeled with an error function and fit to source data for each of the 28 crystals in GRETINA. The measured spectrum was fit simultaneously in the lab frame and Doppler-corrected frame in order to properly account for prompt γ-rays emitted in the laboratory frame. When extracting lifetimes from broadened peaks, the spectra were further divided into three angular groups, each of which have a significantly different peak shape. This distinction enabled us to discriminate true lifetime effects from multiplets or – at lower energies – backscatter peaks from higher transitions. For example, the apparent low-energy structures observed in coincidence with ^{35}Si and ^{35}Al are well reproduced by the simulation of the higher-energy transitions, while the structures in ^{37}Si and ^{39}Si are only reproduced with the assumption of an additional peak with a lifetime effect. Finally, the proximity of these broadened peaks to the γ detection threshold introduces a dependence of the extracted peak intensity on the assumed lifetime. This dependence is included in the evaluation of uncertainties. More details may be found in [19].

TABLE I. Characteristics of the three secondary beams. The momentum spread Δp is the full width at half maximum of the unreacted momentum distribution.

Secondary beam	^{36}Si	^{38}Si	^{40}Si
Mid-target Energy (MeV/u)	97.7(5)	86(1)	79(1)
rate on target[a] (pps)	3100(300)	310(60)	70(20)
$\Delta p/p_0$ (%)	0.6	1.2	2.6
Be target thickness (mg/cm^2)	287(3)	287(3)	376(4)

[a] The uncertainty in the beam rate reflects the rms fluctuation over time, not the measurement uncertainty.

III. THEORY

Large-scale shell model calculations were performed to obtain theoretical level schemes for the residue nuclei, and spectroscopic factors for the overlap between the final and initial states. The calculations were performed using the code NuShellX [20] with two phenomenological effective interactions, SDPF-U [21] and SDPF-MU [7]. These two interactions were derived in different ways, but they both reflect the microscopic picture of the region as described in the introduction. The interactions were developed for calculations with valence protons restricted to the *sd* shell and valence neutrons restricted to the *fp* shell. However, because the odd-A silicon isotopes in this region have low-lying intruder states which we find to be strongly populated in these knockout reactions, we allow 1p-1h neutron excitations across the N=20 gap. This sort of truncation has been used before to calculate states in ^{35}Si with the predecessor to SDPF-U [22], and to calculate states in ^{37}Si with SDPF-MU [23]. The very small resulting spurious center-of-mass contamination is removed by adding a center-of-mass term, multiplied by a factor β_{CM} to the Hamiltonian [24]. This prescription is valid under the assumption that other $1\hbar\omega$ excitations contribute negligibly to the low-lying intruder states. In a sensitivity check, energy levels for intruder states were found to change by $\lesssim 2$ keV for the range $10 \leq \beta_{CM} \leq 50$, indicating that the spurious states were successfully suppressed. We use $\beta_{CM} = 50$ for all 1p-1h calculations in this work. Reduced transition probabilities for $E2$ transitions are calculated using effective charges of $e_p = 1.35$, $e_n = 0.35$ [7], while for $M1$ transitions, we use $g_s = 0.75 g_s^{\rm free}$, $g_\ell^\pi = 1.1$, $g_\ell^\nu = 0.1$ [25].

As described in [26], the cross section for knockout from the initial state i in the A-body system – typically the ground state – to the final state f in the $A-1$-body

system separates into a spectroscopic factor C^2S and a single-particle cross section $\sigma_\alpha^{\rm sp}$:

$$\sigma_\alpha^{fi} = \left(\frac{A}{A-1}\right)^N C^2 S \sigma_\alpha^{\rm sp}, \quad (1)$$

where α labels the quantum numbers n, ℓ, j, t_z of the removed nucleon. The A-dependent factor is a center-of-mass correction to the shell-model spectroscopic factor for a valence particle in oscillator shell N [27]. The single-particle cross section $\sigma_\alpha^{\rm sp}$ is obtained with an eikonal model as described in [26], assuming (i) a normalized single-particle wave function for the removed nucleon and (ii) complex residue- and nucleon-target optical potentials computed from assumed residue and target densities. The residue density distributions are taken from a Hartree-Fock calculation using the SKX Skyrme interaction [28], and the target density is approximated as a Gaussian form with an rms radius of 2.36 fm for both protons and neutrons. If this target density distribution is instead taken from a quantum Monte Carlo calculation [29], the relative importance of the inelastic (stripping) and elastic (diffraction) breakup contributions change at the 5-10% level (the Gaussian form producing more stripping), but the overall single-particle cross sections are unchanged within 1-2%. We use the Gaussian target density for consistency with much previous work.

The normalized radial form factors of the single-nucleon overlaps are calculated in Woods-Saxon potentials whose geometries are adjusted to reproduce the rms radius and energy of each single-particle orbital, obtained with SKX Hartree-Fock calculations [30]. The depth of each Woods-Saxon potential, with its deduced geometry, is then adjusted to reproduce the empirical nucleon separation energy for the final state of interest. All cross sections shown here use this variant of the so-called well-depth prescription. We revisit this prescription for the case of weakly occupied orbits above the Fermi surface when presenting the inclusive and exclusive knockout cross-sections in Section V. Further details of the single-particle cross section calculations are contained in the Supplemental Material at [URL inserted by publisher].

The theoretical, projectile rest-frame parallel momentum distributions of the outgoing knockout residues, which reflect the orbital angular momentum ℓ of the removed nucleon, are calculated with the same interaction and overlap inputs as are detailed above, using the formalism of [31]. The calculated rest frame distributions must be boosted to the laboratory frame for direct comparisons with the measured distributions. As will be discussed in Section VI, in this work each of these symmetric (eikonal) model momentum distributions will be folded with an asymmetric empirical distribution, $\mathcal{F}(p)$ – deduced from measured projectile inelastic scattering events involving target excitation – to account (approximately) for the effects of energy dissipating collisions with the ^{9}Be target. This proposal for treating energy transfer with the target, missing from the eikonal model dynamical description, generates low-momentum tails to the calculated residue distributions with a magnitude consistent with those observed in the experiment. The final, corrected theoretical distributions shown in the figures of this work have been scaled to the integrated number of counts in each experimental distribution.

IV. KNOCKOUT RESIDUE LEVEL SCHEMES

With the exception of ^{35}Si and ^{37}Si, very little was previously known about the level schemes of the knockout residues. $\gamma\gamma$ coincidences, intensity arguments, and comparison with shell model predictions were used to construct the level schemes. Spin-parity assignments are made with the aid of parallel momentum distributions, which are sensitive to the orbital angular momentum of the removed nucleon.

A. ^{35}Si

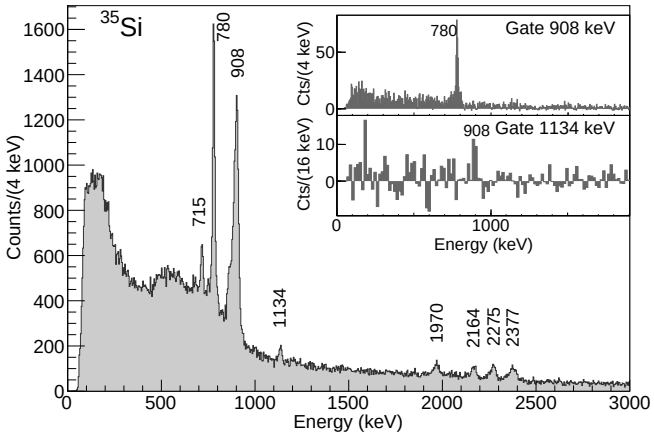

FIG. 1. Doppler-reconstructed γ-ray spectrum detected in coincidence with ^{35}Si. The 908 keV transition is broadened by a lifetime effect of approximately 80 ps. The inset figures show background-subtracted projections of the $\gamma\gamma$ coincidence matrix, gated on the 908 and 1134 keV transitions. The Doppler reconstruction was performed with a velocity $v/c = 0.43$.

TABLE II. Gamma-ray energies, efficiency-corrected intensities, and coincidences for ^{35}Si.

E_γ [keV]	Yield/100 ions	Coincident γ rays	Level [keV]
715(4)	1.9(2)		1688(5)
780(4)	13(1)	908	1688(5)
908(4)	25(2)	780	908(4)
1134(5)	1.5(2)	908	2042(6)
1970(6)	1.4(2)		1970(6)
2164(6)	1.4(2)		2164(6)
2275(6)	2.0(3)		2275(6)
2377(7)	2.5(3)		2377(7)
3611(8)	1.0(2)		3611(8)

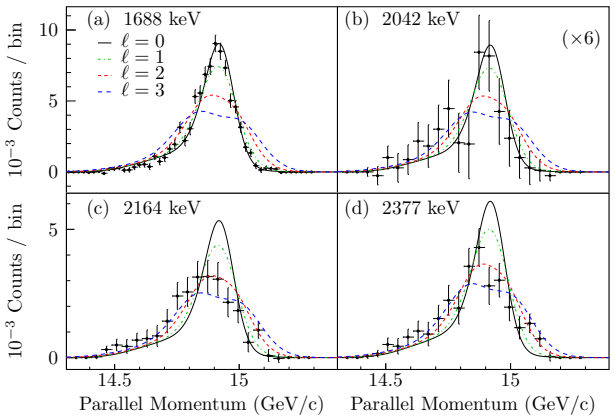

FIG. 2. (Color online) Parallel momentum distributions for the population of levels at 1688, 2042, 2164, and 2377 keV in ^{35}Si by neutron knockout from ^{36}Si. The distribution in (b) has been scaled by a factor of 6.

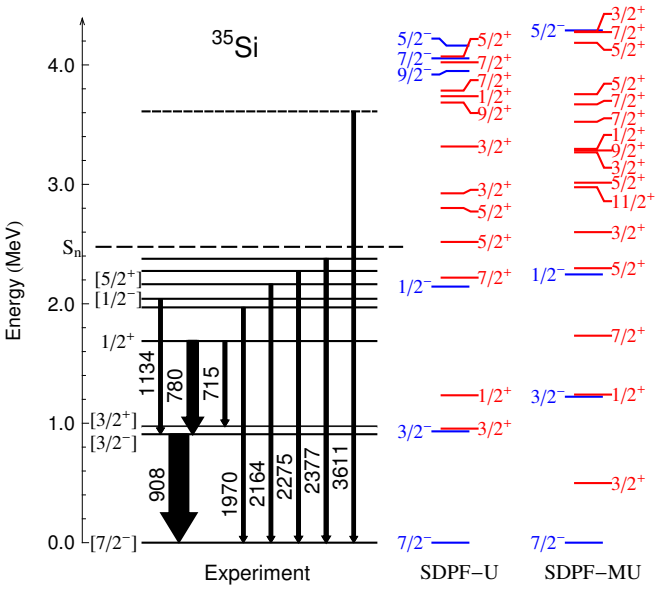

FIG. 3. (Color online) Proposed level scheme for ^{35}Si from this work compared with shell-model calculations (see text for details). The widths of the arrows are proportional to the efficiency-corrected γ-ray intensity.

A previous β decay measurement [22] found three excited states in ^{35}Si: a $3/2^-$ state at 910 keV, a $3/2^+$ state at 974 keV, and a $5/2^+$ state at 2168 keV. The 974 keV state decays predominately by a 64 keV γ-ray transition with a life time of $\tau = 8.5(9)$ ns – too long to be observed in-flight in the current experiment – and so its population could not be deduced here. The ground state was assumed to be $7/2^-$, from systematics and comparison with shell model calculations, also consistent with the long lifetime for the $3/2^+$ state. A recent (d,p) reaction study [10] found an additional state at 2044(7) keV, assigning it to have spin-parity $1/2^-$, as well as providing supporting evidence for the ground state $7/2^-$ assignment.

The γ-ray spectrum in coincidence with outgoing ^{35}Si ions in the current experiment is shown in Figure 1. Two strong peaks at 780 and 908 keV are observed. The latter peak, which we associate with the 910 keV transition from β decay, is broadened, presumably due to a lifetime effect. The lifetime, extracted from a log-likelihood fit of simulated line shapes, is $\tau = 80(20)$ ps. This corresponds to $B(E2; 3/2^- \rightarrow 7/2^-) = 17^{+4}_{-5}$ e^2fm^4, which compares well with shell model values of 14 and 16 e^2fm^4 calculated with SDPF-U and SDPF-MU, respectively.

The 780 keV transition is clearly seen in the inset of Figure 1 to be in coincidence with the 908 keV line, depopulating a state at 1688 keV. While we do not observe the 974 keV $3/2^+ \rightarrow 7/2^-$ transition found in β decay due to its long lifetime, a line at 715 keV is visible, which may connect the 1688 keV and 974 keV states. From the parallel momentum distribution in coincidence with the γ-rays depopulating the 1688 keV state, shown in Figure 2 (a), we determine $\ell = 0$ for the removed nucleon, and assign this state to be $1/2^+$.

The relatively weak transition at 1134 keV likely corresponds to the unplaced 1130 keV transition seen in [22] and the 1134(6) keV transition reported in [10], which was proposed to depopulate a state at 2044 keV. The lower inset of Figure 1 reveals a coincidence with the 908 keV transition, confirming the state at 2044 keV. The momentum distribution gated on the 1134 keV peak, shown in Figure 2 (b), suggests either $\ell = 0$ or 1, consistent with the $1/2^-$ assignment.

The 2164 keV transition seen in β decay is also present in this measurement, and the coincident momentum distribution suggests $\ell = 2, 3$, consistent with the $5/2^+$ assignment. We do not observe the reported 1194 keV transition connecting that state with the 974 keV state, although the reported 30% branching ratio would put that transition at the limit of our sensitivity.

Due to the low neutron separation energy of 2.48(4) MeV [32] in ^{35}Si and the absence of any excited states below 900 keV, it is assumed that the three other transitions near 2 MeV directly populate the ground state, indicating levels at 1970, 2275, and 2377 keV. The resulting level scheme is shown in Figure 3, and the observed transitions are given in Table II.

Surprisingly, Figure 4 shows that we observe one transition at 3611 keV, which must depopulate a state that is unbound to neutron emission by at least 1.1 MeV. Gamma decays which compete with *proton* emission are seen occasionally, as the proton decay may be hindered by the Coulomb barrier (see, for example, [33]). However, γ decays which compete with *neutron* emission are far less common. In general, a strong angular momentum barrier $\ell \geq 4$ is required to hinder the neutron decay, but it is unlikely that an $\ell \geq 4$ state is populated directly in a knockout reaction, due to the expected very low occupation of the neutron $g_{9/2}$ and higher orbitals.

One possible explanation for this situation is the com-

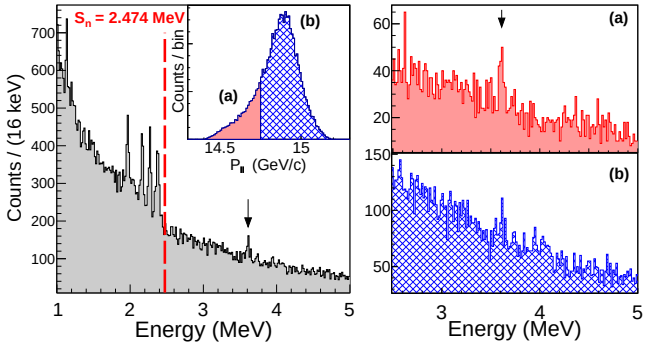

FIG. 4. (Color online) The left panel shows the 3611 keV γ-ray peak (indicated by an arrow) detected in coincidence with ^{35}Si, with an inset showing the gates used on the outgoing parallel momentum distribution. The right panel shows the γ-ray spectra gated on the main peak in the momentum distribution (blue hatches) and the low-momentum tail (solid red). The 3611 keV peak is clearly associated with the tail of the distribution.

bination of a low neutron separation energy in the ^{35}Si parent nucleus (2.48 MeV) and a doubly-magic ^{34}Si daughter nucleus with a high first excited state (2.719 MeV [34]). While a 3.6 MeV state in ^{35}Si is unbound to neutron emission, the ground state of ^{34}Si is the only energetically allowed final state, and so spectroscopic overlaps may significantly hinder the decay. The SDPF-MU (SDPF-U) shell model calculations, combined with eikonal reaction theory, predict knockout to a $5/2^+_3$ state at 3.76 (4.07) MeV with a cross section of 16.8 (13.3) mb. This $5/2^+_3$ state would necessarily contain a neutron hole in the *sd* shell, and could only decay by the emission of a $d_{5/2}$ neutron, resulting in a 2p-2h configuration dominated by two holes in the deeply-bound neutron $d_{5/2}$ orbit. Such a configuration should have a small overlap with the ground state in ^{34}Si – which has a large contribution of 0p-0h configurations [34] – leading to a significantly hindered neutron decay. The γ decay, on the other hand, would be a fast $5/2^+ \rightarrow 7/2^-$ $E1$ decay, and could potentially compete with the neutron emission. Comparing the calculated and measured cross sections, based on the intensity of the 3611 keV γ-ray (see Table VIII), the γ branching ratio would be on the order of 5-10%.

A second explanation could be that this state is weakly populated in a more complicated multi-step reaction pathway. To estimate the yield from such a higher-order removal mechanism, we assume a two-step reaction in which the incident ^{36}Si is first excited to its first 2^+ state, and a neutron is then removed. The details of this calculation are given in an appendix. Based on this two-step model, the most likely final-state candidates are the $7/2^+_1$ and $5/2^+_2$ states (see Figure 3), with estimated cross sections of 0.29 and 0.21 mb, respectively. These two-step estimates are of the same order as the experimental 3611 keV state cross section of 0.8(2) mb.

An additional piece of information is given by the momentum distribution associated with the population of this state. The statistics are insufficient to obtain a background-subtracted momentum distribution for the 3611 keV γ-ray line, as was done for the states in Figure 2. However, when the γ-ray spectrum is gated on high- and low-momentum regions of the outgoing momentum distribution, as shown in the right panel of Figure 4, it is clear that the 3611 keV line results predominantly from events with residue momenta in the tail of the momentum distribution. As will be discussed in Section VI, the low-momentum tail is associated with more inelastic reactions, which would be consistent with a multi-step process. However, the direct knockout of a more deeply-bound $d_{5/2}$ neutron could potentially also produce a distribution with a significant tail.

Clearly, if the $7/2^+_1$ and $5/2^+_2$ states could be identified independently and their energies found to be different from 3.6 MeV, then these observations would favor the direct process.

B. ^{35}Al

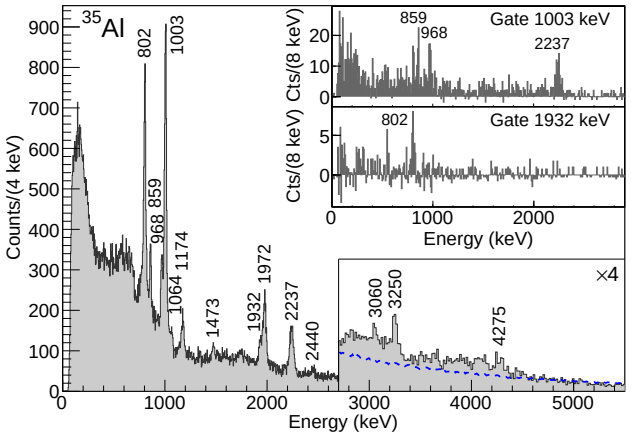

FIG. 5. (Color online) Doppler-reconstructed γ-ray spectrum detected in coincidence with ^{35}Al. The section of the spectrum in the box labeled "×4" has been rebinned by a factor 4. The blue dashed line shows the fitted background, suggesting a peak at 4275 keV. The inset in the upper-right shows background-subtracted projections of the $\gamma\gamma$ coincidence matrix, gated on the 1003 and 2237 keV transitions. The Doppler reconstruction was performed with a velocity $v/c = 0.42$.

The nuclide ^{35}Al was previously studied by Coulomb excitation, yielding one transition at 1020(8) keV [35]. The ground state is assumed to be $5/2^+$ from shell model calculations and systematics, and so the spin of the Coulomb-excited state could be anything from 1/2 to 9/2.

In this work, we observe many transitions and coincidences, shown in Figure 5 and tabulated in Table III. The two strongest transitions, at 802 and 1003 keV, are not in coincidence with each other and are assumed to feed the ground state. Transitions at 859, 968, and 2237 keV are

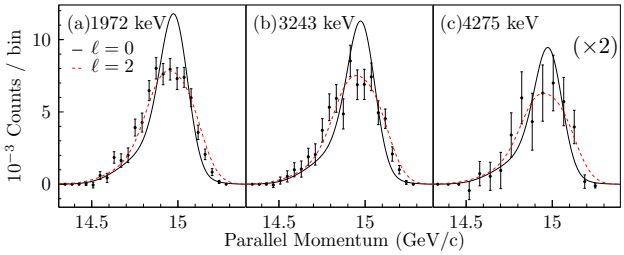

FIG. 6. (Color online) Parallel momentum distributions for the population of levels at 1972, 3243, and 4275 keV in ^{35}Al by proton knockout from ^{36}Si. The distribution in (c) has been scaled by a factor of 2.

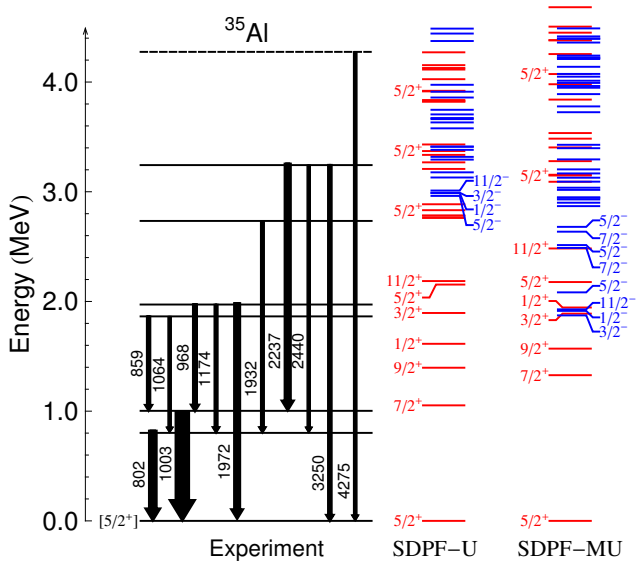

FIG. 7. (Color online) Proposed level scheme for ^{35}Al from this work compared with shell-model calculations (see text for details). The width of the arrows is proportional to the efficiency-corrected γ-ray intensity.

TABLE III. Gamma-ray energies, efficiency-corrected intensities, and coincidences for ^{35}Al. Levels marked with an asterisk are tentative.

E_γ [keV]	Yield/100 ions	Coincident γ rays	Level [keV]
802(4)	10(1)	1923	802(4)
859(4)	3.6(3)	1003	1864(5)
968(4)	4.4(3)	1003	1972(4)
1003(4)	19(1)	859, 968, 2237	1003(4)
1064(4)	0.8(2)		1864(5)
1174(5)	2.8(3)		1972(4)
1473(5)	1.1(2)		
1932(6)	2.5(3)	802	2734(7)
1972(6)	7.5(5)		1972(4)
2237(6)	7.8(6)	1003	3243(5)
2440(7)	1.4(2)		3243(5)
3060(8)	1.6(4)		
3250(8)	3.3(4)		3243(5)
4275(9)	3(1)		4275(9)*

found to be in coincidence with the 1003 keV transition, shown in the inset of Figure 5, and we place them depopulating levels at 1864, 1972, and 3243 keV, respectively. Transitions at 1064, 1174, and 2440 keV each differ from the previously mentioned transitions by approximately 200 keV and, although a coincidence is not observed, we tentatively assign these transitions to connect the levels at 1862, 1972 and 3243 keV to the level at 802 keV. The transition at 1932 keV is in coincidence with the 802 keV transition, as shown in the inset of Figure 5, and it is placed depopulating a state at 2734 keV. The transition at 1972 keV is not observed to have any coincident transitions and we place it connecting the level at 1972 keV to the ground state. Likewise, we place the transition at 3250 keV connecting the level at 3243 keV to the ground state. The neutron separation energy for ^{35}Al is 5244(92) keV [32], so the transition at 4275 keV, shown in Figure 11 on top of an exponential background, could populate the ground state or one of the lowest two excited states. In the absence of any observed coincidences, we tentatively place the 4275 keV transition feeding the ground state.

Momentum distributions in coincidence with decays from the proposed levels at 1972, 3243, and 4275 keV are shown in Figure 6, and the momentum distribution for the population of the ground state, obtained by subtraction, is shown in Figure 25(c). All of these distributions are consistent with the removal of a proton with $\ell = 2$.

C. ^{37}Si

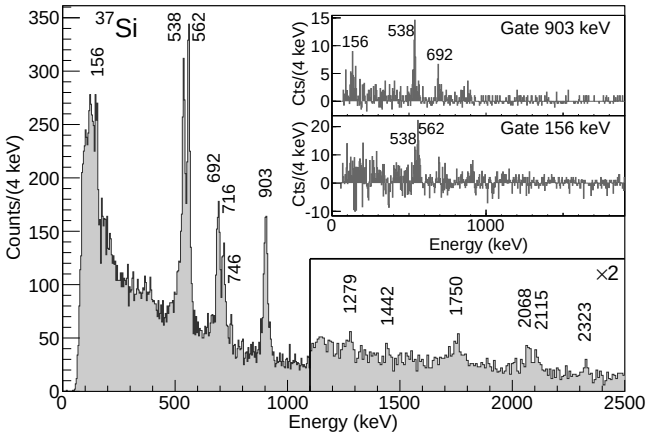

FIG. 8. Doppler-reconstructed γ-ray spectrum detected in coincidence with ^{37}Si. The section of the spectrum in the box labeled "×2" has been rebinned by a factor of 2. The inset shows the background-subtracted projections of the $\gamma\gamma$ coincidence matrix, gated on the peaks at 156 and 903 keV. The Doppler reconstruction was performed with a velocity $v/c = 0.40$.

The structure of ^{37}Si has been previously studied by Coulomb excitation [35], in which the authors tentatively

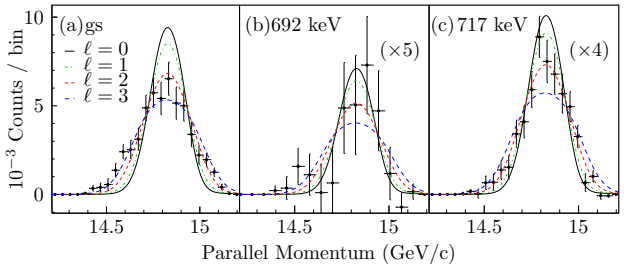

FIG. 9. (Color online) Parallel momentum distributions for the population of the ground state and excited states at 692 and 717 keV in ^{37}Si by neutron knockout from ^{38}Si. Note that the ground state distribution includes both the $5/2^-_1$ and $7/2^-_1$ states. The distributions in (b) and (c) have been scaled by factors of 5 and 4, respectively.

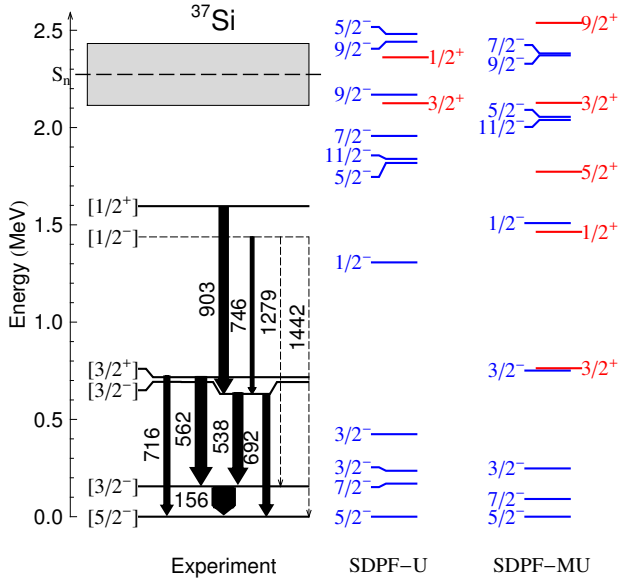

FIG. 10. (Color online) Level scheme for ^{37}Si from this work compared with shell-model calculations (see text for details). The width of the arrows is proportional to the γ-ray intensity. Fine dashed lines indicate tentative levels and transitions, while the thicker dashed line labeled S_n indicates the neutron separation energy, with the gray shaded area indicating the uncertainty.

proposed a level at 1437(27) keV, and also by the β decay of ^{37}Al [23], in which levels at 68, 156, 717, and 1270 keV were proposed. The authors mention in [35] that the 1437 keV level is uncertain and could be due to a stripping reaction, rather than inelastic scattering. As no transition near 1437 is seen in the present work or the β decay, and the $2^+_1 \rightarrow 0^+_1$ transition in ^{36}Si lies at 1408 keV [36, 37], we do not include this level in the ^{37}Si level scheme. The levels from β decay at 717 and 1270 keV were tentatively assigned to $3/2^+$ and $5/2^+$, respectively, based on $\log(ft)$ values.

Unlike in ^{35}Si, where the $7/2^-$ ground state is well separated from the first excited states, the shell model predicts low-lying $3/2^-$ and $5/2^-$ states, which correspond primarily to seniority $v = 3$ $(f_{7/2})^3$ configurations, with the $5/2^-$ predicted to be the ground state. This suggests that, whatever the spin-parity of the ground state, the other two low-lying states may be nanosecond isomers. Additionally, these states allow the $3/2^+$ intruder state to decay by a fast $E1$, making the population of the $3/2^+$ state detectable.

TABLE IV. Gamma-ray energies, efficiency-corrected intensities, and coincidences for ^{37}Si. Levels and transitions marked with an asterisk are tentative.

E_γ [keV]	Yield/100 ions	Coincident γ rays	Level [keV]
156(3)	36(5)	538, 562	156(3)
538(4)	11(1)	156, 903	693(4)
562(4)	13(1)	156	717(4)
692(4)	6.6(9)	903	693(4)
716(4)	5.3(8)		717(4)
746(4)	0.8, 6)		1438(6)*
903(4)	10(1)	538, 692	1596(5)
1279(5)*	1.4(5)		1438(6)*
1442(5)*	0.6(5)		1438(6)*
1750(6)	2.3(7)		
2068(6)	1.9(6)		
2115(6)	1.8(6)		
2323(6)*	0.8(5)		

The γ-ray spectrum for the current measurement is shown in Figure 8. We observe transitions at 562 and 716 keV, consistent with the β decay findings. The parallel momentum distribution in coincidence with a decay from the 716 keV level (Figure 9(c)) suggests a removal of an $\ell = 2$ neutron, consistent with the $3/2^+$ assignment. As mentioned above, the $3/2^+_1$ state is expected to decay to the low-lying $3/2^-_1$ and $5/2^-_1$ states. The significant direct population of the state at 156 keV (see Table VIII) suggests that that state is the $3/2^-_1$ and the ground state is $5/2^-_1$.

The transition at 156 keV is also seen, although it is broadened by a lifetime effect. From simulation, we estimate the lifetime of the 156 keV state to be $\tau = 4.4(10)$ ns. Assuming a pure $M1$ transition, which is not unreasonable for such a low-energy transition, this corresponds to $B(M1; 3/2^-_1 \rightarrow 5/2^-_1) = 3.4^{+1.0}_{-0.7} \times 10^{-3}\ \mu^2_N$, which may be compared with shell model values of 1×10^{-3} and $1.5 \times 10^{-2}\ \mu^2_N$ for SDPF-U and SDPF-MU, respectively.

In addition, we observe two new transitions at 538 and 692 keV, which are also separated by approximately 156 keV. We place these transitions depopulating a state at 692 keV. From the parallel momentum distribution shown in Figure 9(b) and comparison to shell model calculations, we assign this level to be $3/2^-$. We observe that this $3/2^-$ level is nearly degenerate with the lowest $3/2^+$ level, as in ^{35}Si and as predicted by SDPF-MU. In the calculations, the lowest-lying $3/2^-_1$ state is generated primarily by a neutron $(f_{7/2})^3$ configuration, while

the $3/2_2^-$ state is generated primarily by an $(f_{7/2})^2 p_{3/2}$ configuration.

A transition at 903 keV is observed to be in coincidence with the 692 and 538 keV transitions (see the inset in Figure 8), and it is placed connecting a level at 1596 keV to the level at 693 keV. The corresponding parallel momentum distribution in Figure 25(d) suggests $\ell = 0$ or 1. Considering its strong population and comparing to the shell model and the ^{35}Si level scheme, we assign this state to be $1/2^+$.

A possible transition at 1279 keV could be associated with the $5/2^+$ level from β decay. In that work, the 1270 keV level fed the ground state and excited states at 68 and 156 keV with roughly equal branching ratios, indicating that we should see transitions at 1202 and 1115 keV, which we do not. As an alternative, we note that the difference between the 1279 and 746 keV transitions is 533 keV, which agrees within uncertainty with the energy difference between the 692 and 156 keV levels, suggesting a level at 1438 keV. Indeed, we also see a possible very weak transition at 1442 keV, which would connect this level to the ground state. This state would be a candidate for the $1/2_1^-$ level predicted in both shell model calculations in Figure 10, which would decay by $M1$ to both $3/2^-$ states and by $E2$ to the $5/2^-$ ground state. Decay to the $3/2_1^+$ intruder state would be hindered because the predominant single-particle configurations, $(d_{3/2})^{-1}(f_{7/2})^4$ and $(f_{7/2})^2 p_{1/2}$ cannot be connected with a one-body transition. We therefore tentatively place the $1/2^-$ state in the level scheme at 1438 keV.

The additional observed transitions at 1750, 2068, 2115 keV and a possible transition at 2323 keV are not placed in the level scheme, although due to the neutron separation energy at 2250(100) keV, they will very likely only feed the ground state or other members of the low-lying multiplet. The observed γ-rays are tabulated in Table IV and the proposed level scheme is shown in Figure 10.

D. ^{37}Al

TABLE V. Gamma-ray energies, efficiency-corrected intensities, and coincidences for ^{37}Al. Levels marked with an asterisk indicate a tentative assignment.

E_γ [keV]	Yield/100 ions	Coincident γ rays	Level [keV]
755(6)	4.5(12)	775	1530(7)
775(4)	23(2)	755	775(4)
861(4)	2.6(10)		
1255(5)	7.0(13)		1255(5)*
1393(5)	6.7(13)		1393(5)*
1612(5)	3.2(11)		
2558(7)	7.3(19)	775	3327(8)
2722(7)	3.8(16)		
3321(8)	4.7(15)		3327(8)

No previous data exist on excited states of ^{37}Al. In this work, we observe a strong transition at 775 keV. This transition is seen to be coincident with the transition at 2558 keV and with itself. Since the coincidence spectrum is background-subtracted, this indicates that there is another transition with a nearly identical energy. In fact, the 775 keV peak has a shoulder at low energy, suggesting a possible second peak. A fit with two Gaussians gives a best description with peaks at 775 and 755 keV, suggesting levels at 775 and 1530 keV, as shown

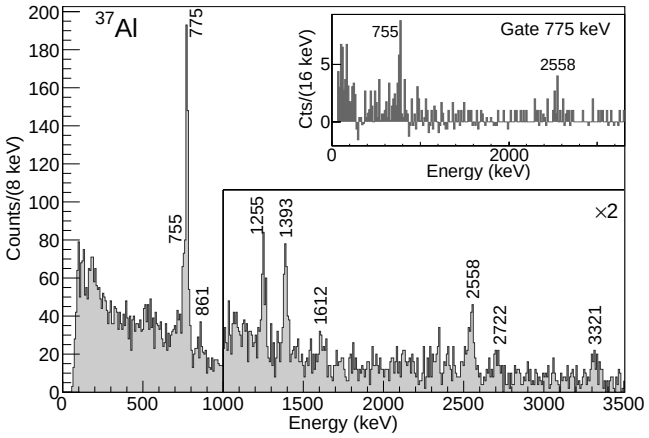

FIG. 11. Doppler-reconstructed γ-ray spectrum detected in coincidence with ^{37}Al. The section of the spectrum in the box labeled "×2" has been scaled by a factor of 2. The inset shows the background-subtracted projection of the $\gamma\gamma$ coincidence matrix, gated on the peak at 775 keV. The Doppler reconstruction was performed with a velocity $v/c = 0.40$.

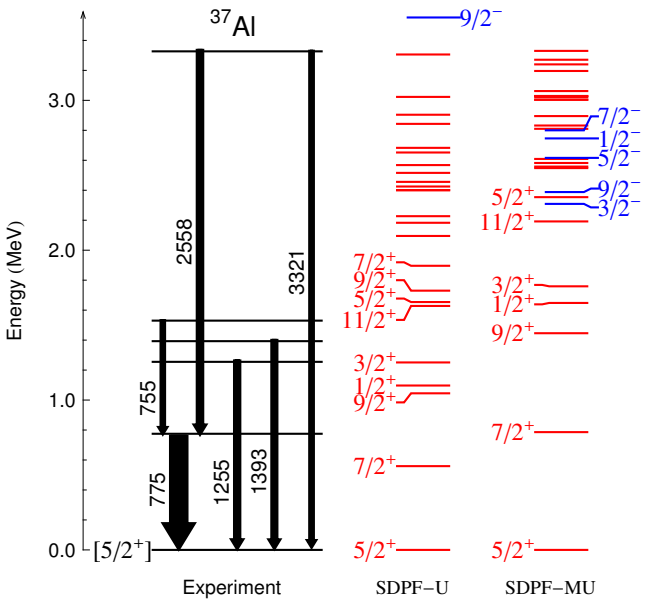

FIG. 12. (Color online) Proposed level scheme for ^{37}Al from this work compared with shell-model calculations (see text for details). The width of the arrows is proportional to the efficiency-corrected γ-ray intensity.

in Figure 12. The transition at 3321 keV agrees within uncertainty with the sum of 775 and 2558, and so we place that transition connecting a level at 3327 keV with the ground state. The transitions at 1255 and 1393 keV are not observed in coincidence with either peak in the doublet at 775 keV, and they are not expected to feed the state at 3327, due to the neutron separation energy at 4210(160) keV [32]. We therefore tentatively place the 1253 and 1393 keV transitions directly populating the ground state. Observed transitions at 861, 1612, and 2722 keV are not placed in the level scheme. From comparison with the shell model calculations, one would expect that the level at 775 keV to be weakly populated in a knockout reaction. We note that the intensities of these three unplaced transitions could account for most of the remaining population of the 775 keV state, and bring the results into better agreement with the shell model.

E. ^{39}Si

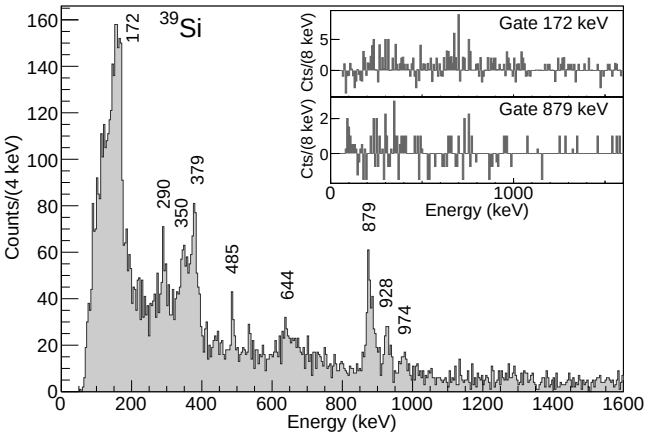

FIG. 13. Doppler-reconstructed γ-ray spectrum detected in coincidence with ^{39}Si. The Doppler reconstruction was performed with a velocity $v/c = 0.38$. The inset shows the background-subtracted $\gamma\gamma$ coincidence matrix gated on the peaks at 172 and 879 keV, revealing no strong coincidences with either peak.

The excited states of ^{39}Si have been studied previously by fragmentation of ^{40,41}P and ^{42,43}S [38]. Sohler *et al.* observed prominent peaks at 163(12) and 397(14) keV, as well as several other more weakly-populated transitions, and their high efficiency allowed them to establish several $\gamma\gamma$ coincidences. As in ^{37}Si, the shell model predicts two low-lying $v = 3$ states for ^{39}Si, suggesting the presence of two isomers. As described earlier, these states allow the prompt decay of the $3/2^+$ intruder state.

In the present work, we observe a pronounced structure at 172 keV, likely broadened by a lifetime effect. From simulation we estimate the lifetime of the 172 keV transition to be τ=1.3(2) ns. Assuming a pure $M1$ transition $7/2^- \rightarrow 5/2^-$, as discussed below, this corresponds to

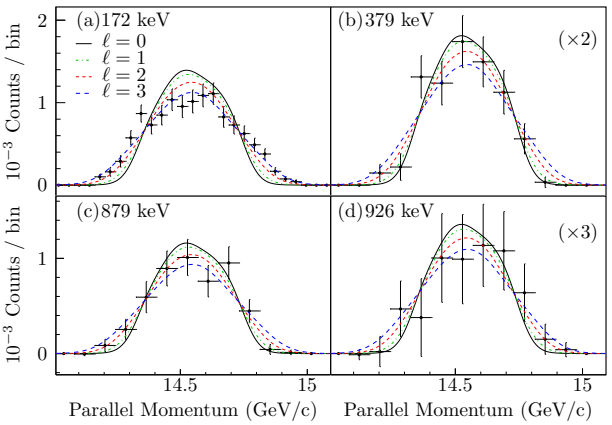

FIG. 14. (Color online) Parallel momentum distributions gated on γ-ray transitions in ^{39}Si (no feeding subtraction). The distributions in (b) and (d) have been scaled by factors of 2 and 3, respectively.

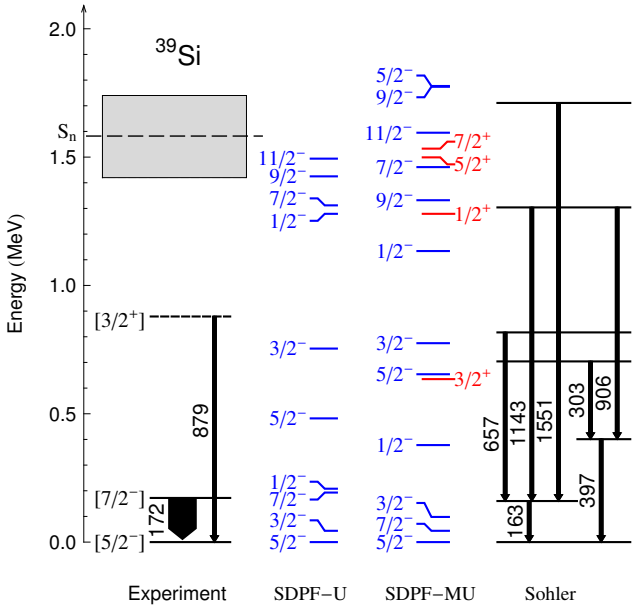

FIG. 15. (Color online) The left side shows the proposed level scheme for ^{39}Si. The right side is the level scheme proposed by Sohler *et al.* [38]. In the left level scheme, the width of the arrows in proportional to the efficiency-corrected γ-ray intensity. As described in the text, the levels could have an offset if the lowest $3/2^-$ state lies below the $5/2^-$.

$B(M1; 7/2^-_1 \rightarrow 5/2^-_1) = 8.6^{+1.5}_{-1.2} \times 10^{-3}\ \mu_N^2$, compared to shell model predictions of 3×10^{-3} and $6 \times 10^{-3}\ \mu_N^2$ for SDPF-U and SDPF-MU, respectively.

In [38], the γ-ray spectrum resulting from proton knockout from ^{40}P was dominated by the 163 keV transition, which we associate with our 172 keV transition due to the fact that the lifetime effect – imperceptible with their energy resolution – shifts the centroid of the peak to a slightly lower energy. Using the SDPF-MU spec-

TABLE VI. Gamma-ray energies, efficiency-corrected intensities, and coincidences for ^{39}Si. Levels marked with an asterisk are tentative.

E_γ [keV]	Yield/100 ions	Coincident γ rays	Level [keV]
172(5)	39(6)		172(5)
290(3)	4(1)		
350(3)	6(2)		
379(3)	10(2)		
485(4)	3(1)		
644(4)	3(1)		
879(4)	12(2)		879(5)*
928(4)	5.4(11)		
974(4)	2.5(9)		

troscopic factors and single-particle cross sections from eikonal theory with a quenching factor R=0.4 [30], we estimate the cross sections for one proton knockout from ^{40}P to the lowest-lying states in ^{39}Si to be $5/2^-_1$: 1.8 mb, $7/2^-_1$: 1.1 mb, $3/2^-_1$: 0.1 mb, $1/2^-_1$: 0.06 mb, $5/2^-_2$: 0.4 mb, $3/2^-_2$: 0.2 mb. (Here, we assume a 2^- ground state, although the results are similar for a 3^- ground state.) This suggests that their 163 keV transition depopulates either the $5/2^-_1$ or $7/2^-_1$. Since we also populate this transition strongly in one-neutron knockout, it is most likely that this transition depopulates the $7/2^-_1$ state. The parallel momentum distribution in coincidence with this transition shown in Figure 14(a) suggests $\ell = 2, 3$ for the removed nucleon, in support of this assignment. Due to the low energy of the transition, it most likely proceeds by $E1$ or $M1$. From comparison with the shell model level schemes, the most likely candidate for the final state is $5/2^-$. The shell-model calculations also predict a low-lying $3/2^-$ state which, within the uncertainty of the calculations, could lie below the $5/2^-$ state, making it the ground state. If this were the case, the levels proposed here would be shifted up in energy by the gap between the $3/2^-$ and the $5/2^-$ states.

We also expect to preferentially populate $3/2^+$, $1/2^+$ and $3/2^-$ states with the knockout reaction. The next-strongest transition at 879 keV has a corresponding parallel momentum distribution shown in Figure 14(c) that suggests $\ell = 2, 3$, so we tentatively assign that transition to depopulate a $3/2^+$ level. By comparison with the shell model, the most probable final state for the decay of the $3/2^+$ state would be the $5/2^-$ ground state, as the population of the $7/2^-$ state would require a slower $M2$ transition, and the population of the $3/2^-$ and $1/2^-$ states would be hindered by their strong admixtures of $(f_{7/2})^4 p_{3/2}$ and $(f_{7/2})^4 p_{1/2}$, respectively. We therefore tentatively place the $3/2^+$ level at 879 keV, connecting to the $5/2^-$ ground state. The momentum distribution in Figure 14(b) in coincidence with the 379 keV transition suggests a slight preference for $\ell = 0$ or 1 but the statistics are weak and without additional information from $\gamma\gamma$ coincidences, the placement in the level scheme is unclear.

Additional lines at 290, 350, 485, 928, and 974 keV, as well as a broad structure around 644 keV, which likely corresponds to an unresolved multiplet, are likewise not placed in the level scheme. The inset panel in Figure 13 shows the $\gamma\gamma$ coincidence matrix gated on the two strongest peaks at 172 and 879 keV, revealing no clear coincidences. The most prominent structure in the 172 keV coincidence spectrum is centered around 750 keV, which does not correspond to any transition observed in singles. This supports the interpretation that these transitions depopulate states which are directly populated in the knockout reaction.

F. ^{39}Al

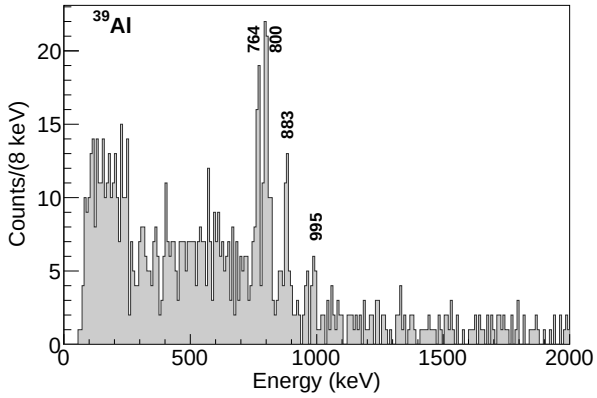

FIG. 16. Doppler-reconstructed γ-ray spectrum detected in coincidence with ^{39}Al. The Doppler reconstruction was performed with a velocity $v/c = 0.39$.

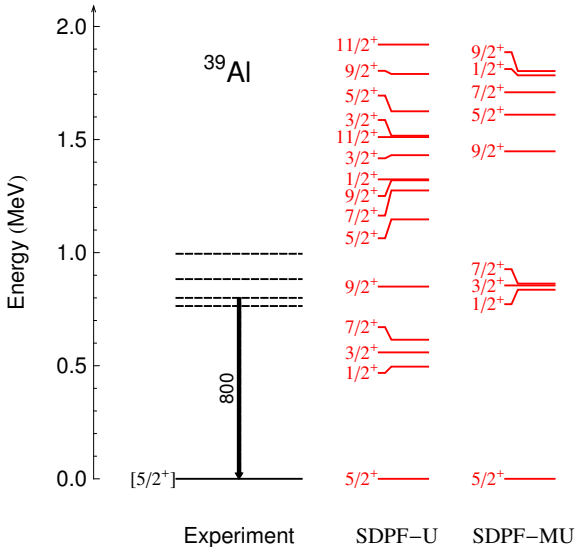

FIG. 17. (Color online) Proposed level in ^{39}Al at 800 keV with dashed lines indicating the possible locations of other levels, assuming ground-state transitions. The center and right figures are shell-model calculations (see text for details).

TABLE VII. Gamma-ray energies, efficiency-corrected intensities, and coincidences for ^{39}Al.

E_γ [keV]	Yield/100 ions	Coincident γ rays	Level [keV]
764(8)	10(4)		
800(8)	12(4)		800(8)
883(8)	9(4)		
995(8)	1(2)		

No previous measurements of the excited states of ^{39}Al exist. In the current measurement we observe three transitions, at 764, 800, and 883 keV, and a possible peak at 995 keV. The low statistics in this setting preclude any $\gamma\gamma$ coincidence measurement. The 800 keV transition is the most intense and we assign it populating the ground state. The other transitions are not placed in the level scheme.

V. KNOCKOUT CROSS SECTIONS

A. Inclusive cross sections

The inclusive knockout cross sections for the population of all bound final states is obtained using

$$\sigma_{\rm ko} = \frac{N_{ko}}{N_p n_t \epsilon}. \quad (2)$$

Here N_p is the number of incident projectiles, N_{ko} is the number of detected knockout residues, n_t is the areal target density in atoms/mb and ϵ is the detection efficiency for the outgoing fragment. In all knockout settings, the entire knockout residue momentum distribution was within the acceptance of the S800 spectrograph, so the efficiency is $\epsilon \approx 1$ within the precision of the measurement. For those same settings, the unreacted projectiles were not entirely within the acceptance of the S800. The incident rate was determined by the count rate on a scintillator located before the target in the object position of the S800 analysis beam line, scaled to a calibration run with the S800 acceptance centered on the unreacted projectile. The dominant source of uncertainty in this measurement is the variation with time in the transmission and composition of the incoming beam, which is estimated by calculating the cross section independently for each hour-long run, and calculating the root-mean-squared (rms) deviation of these independent measurements.

The results of these measurements are shown in Figure 18 and in Table VIII. Figure 18 also shows the summed theoretical knockout cross sections to all bound shell model final states up to the neutron separation energy. Also shown are the results when these theoretical values are scaled by reduction factors; $R(\Delta S) = (0.83,0.86,0.91)$ for neutron removal and $R(\Delta S) = (0.39,0.36,0.31)$ for proton removal from (^{36}Si,^{38}Si,^{40}Si). These values are deduced from a linear fit to the systematics of [30]. The resulting agreement with the experimental values, following this scaling, confirms the consistency of these data with (and adds additional points to) these cross section systematics with increasing neutron-proton number asymmetry [30].

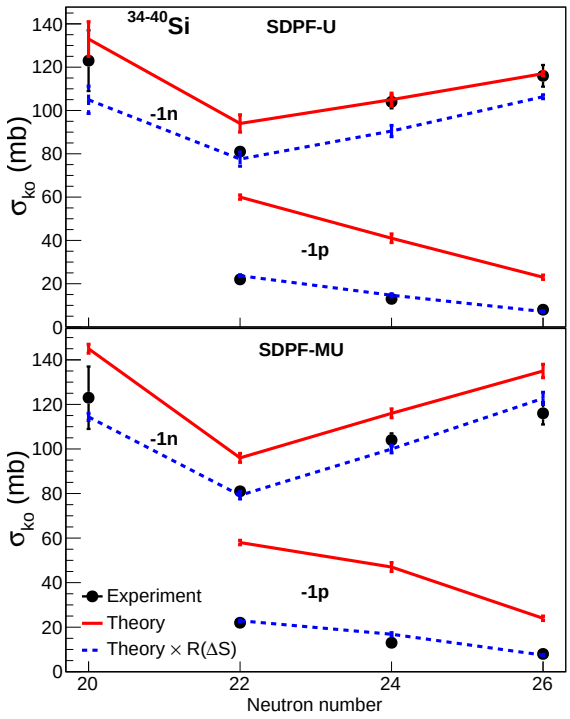

FIG. 18. (Color online) Inclusive one-neutron and one-proton knockout cross sections from silicon isotopes to all bound final states as a function of the neutron number N of the projectile. The measured values (black points) are compared with theoretical predictions (connected by the solid red line) and with these theoretical predictions scaled by a reduction factor $R(\Delta S)$ deduced from knockout systematics [30] and ranging from 0.83-0.91 for neutron knockout and from 0.31-0.39 for proton knockout (see Figures 19-24). The theoretical error bars indicate the sensitivity when varying the neutron separation energy by $\pm$500 keV. The experimental value for ^{34}Si is taken from [39]

We note that, within the shell model calculations, the decrease in the neutron knockout cross section from ^{34}Si to ^{36}Si is due to the filling of the neutron sd shell at ^{34}Si, adding the shell gap energy of $\epsilon(f_{7/2}) - \epsilon(d_{5/2})$ to the separation energy for population of $d_{5/2}$ hole states and moving this hole strength above the low first neutron threshold in ^{35}Si.

B. Exclusive cross sections

The partial cross sections to excited states were deduced from the feeding-corrected γ-ray intensities. The cross section to the ground state is obtained by subtract-

TABLE VIII. Total and partial knockout cross sections for each of the knockout reactions studied.

	σ_{ko}[mb]	E_{final}[keV]	J^{π}_{final}	σ_{part}[mb]
^{36}Si→^{35}Si	81(2)	0	$[7/2^-]$	52(4)[a]
		908	$[3/2^-]$	8(3)
		974	$[3/2^+]$	[b]
		1688	$1/2^+$	13(1)
		1979		1.1(2)
		2042	$[1/2^-]$	1.3(2)
		2164	$[5/2^+]$	1.1(2)
		2275		1.6(2)
		2377		2.1(2)
		3611		0.8(2)
^{38}Si→^{37}Si	104(3)	?[c]	$[7/2^-]$[d]	47(9)
		156	$[3/2^-]$	9(7)
		692	$[3/2^-]$	7(3)
		717	$[3/2^+]$	19(2)
		1438	$[1/2^-]$	3(1)
		1596	$[1/2^+]$	10(1)
^{40}Si→^{39}Si	116(5)	?[c]	$[3/2^-]$[d]	29(20)
		172	$[7/2^-]$	49(7)
^{36}Si→^{35}Al	22(1)	0	$[5/2^+]$	13(2)
		802		1.0(7)
		1003		0.8(9)
		1862		1.0(2)
		1972		3.2(5)
		2731		0.5(1)
		3243		2.6(3)
		4275		0.5(1)
^{38}Si→^{37}Al	13(1)	0	$[5/2^+]$	7(2)
		775		1.5(10)
		1253		0.9(2)
		1393		0.9(2)
		3327		1.6(6)
^{40}Si→^{39}Al	8(2)	0	$[5/2^+]$	5(2)
		800		0.9(4)

[a] Includes population of the $3/2^+_1$ isomer.
[b] Not seen due to long lifetime (see text).
[c] Low lying level (energy is unknown).
[d] Includes (presumably weak) population of the $5/2^-_1$ state.

ing the cross section to all excited states from the total cross section. Of course this means that all isomeric states are included in the ground state cross section for the present measurement. In the case of unplaced γ transitions, the ground state cross section is taken to be the average of the maximal and minimal feeding scenarios, and the cross sections for these unplaced transitions are added in quadrature to the ground state uncertainty. Figures 19-24 compare the measured and calculated partial cross sections, the latter obtained using SDPF-U and SDPF-MU level energies and spectroscopic factors.

Proton knockout, for all three secondary beams, is dominated by population of the $5/2^+$ ground states in ^{35,37,39}Al, consistent with the theoretical predictions, although we do not observe the predicted moderate population of the second $5/2^+$ state in ^{37}Al. This indicates

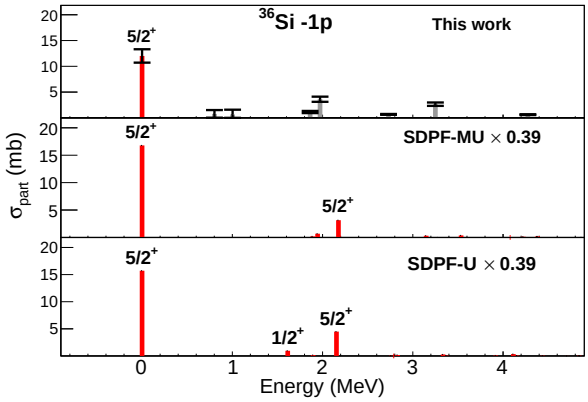

FIG. 19. (Color online) One proton knockout cross section to final states in ^{35}Al. Experimental data are shown in the top panel, and theoretical predictions are shown in the bottom two panels.

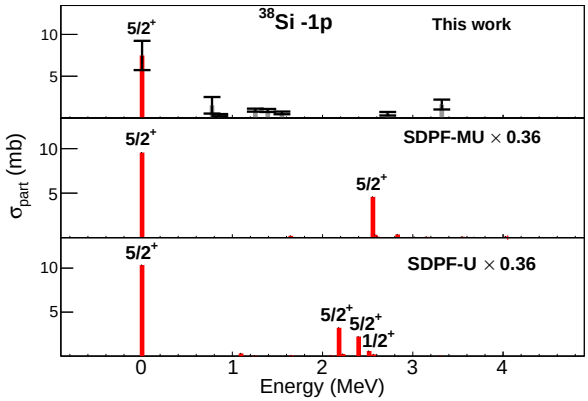

FIG. 20. (Color online) One proton knockout cross section to final states in ^{37}Al. Experimental data are shown in the top panel, and theoretical predictions are shown in the bottom two panels.

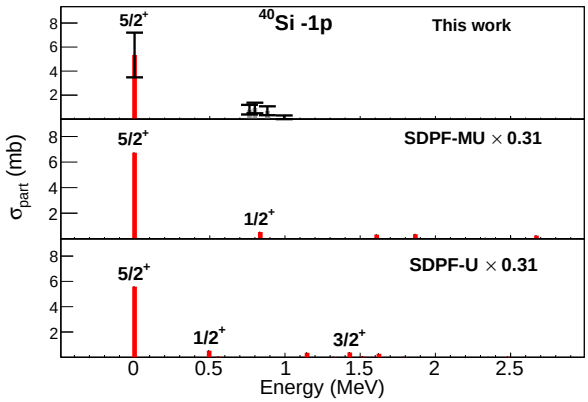

FIG. 21. (Color online) One proton knockout cross section to final states in ^{39}Al. Experimental data are shown in the top panel, and theoretical predictions are shown in the bottom two panels.

that the Z=14 sub-shell closure remains relatively good

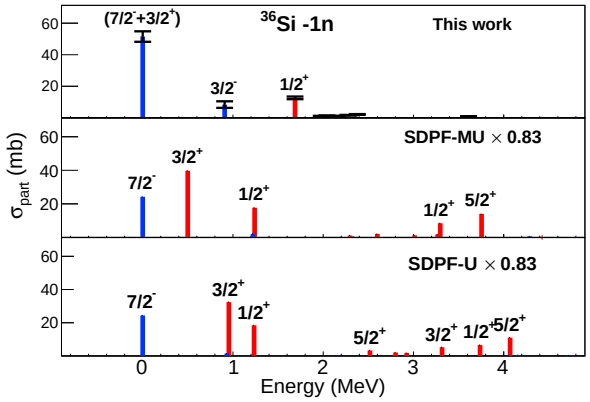

FIG. 22. (Color online) One neutron knockout cross section to final states in ^{35}Si. Experimental data are shown in the top panel, and theoretical predictions are shown in the bottom two panels.

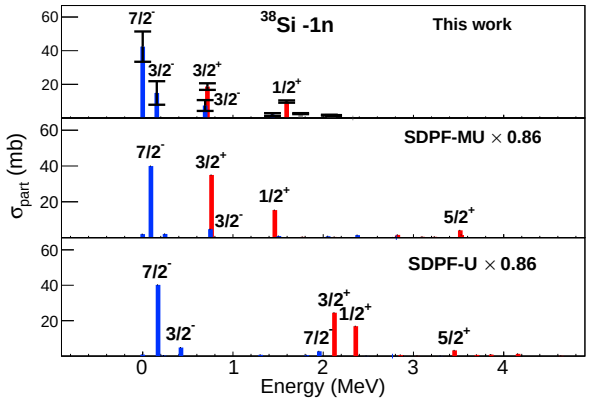

FIG. 23. (Color online) One neutron knockout cross section to final states in ^{37}Si. Experimental data are shown in the top panel, and theoretical predictions are shown in the bottom two panels.

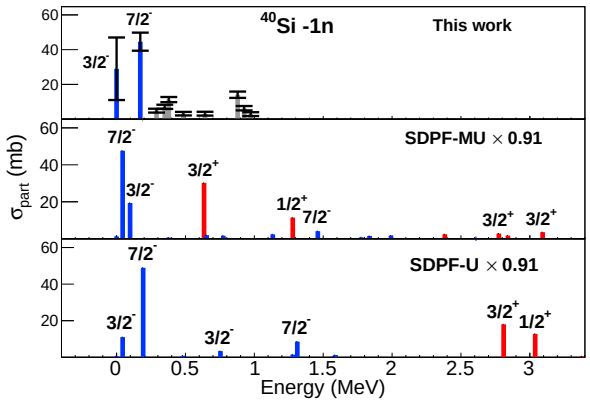

FIG. 24. (Color online) One neutron knockout cross section to final states in ^{39}Si. Experimental data are shown in the top panel, and theoretical predictions are shown in the bottom two panels.

up to ^{40}Si, although as shown in [38], a perfect sub-shell closure, obtained by restricting protons to the $d_{5/2}$ orbital, produces qualitatively incorrect results. We note that because the shell model calculations restrict protons to the *sd* shell, only positive-parity states are accessible in the model space.

The situation is different for neutron knockout. For all three secondary beams, there is significant population of excited states with spin-parity $J^\pi \neq 7/2^-$. For positive-parity states, this indicates the narrowing of the N=20 gap, generating low-lying 1p-1h excitations. For negative-parity states, this indicates the presence of excitations across the N=28 gap in the ground states of ^{36,38,40}Si.

In neutron knockout from ^{36}Si, shown in Figure 22, the experimental cross section distribution is similar to both theoretical predictions, with the exception of the missing experimental strength to the first $3/2^+$ state in ^{35}Si. As mentioned previously, this state is an isomer and we cannot distinguish its population from the population of the ground state.

In ^{37}Si, low-lying $3/2^-$ and $5/2^-$ states allow the $3/2^+_1$ state to decay by a fast $E1$ transition. Thus, we can measure the knockout cross section to the $3/2^+_1$ state and find it to be in agreement with the shell model prediction although, as seen in Figure 10, SDPF-U does not correctly predict the energies of even-parity states.

Finally, in ^{39}Si the present ambiguity of the level scheme hinders the determination of the cross section to the lowest $3/2^-$ state, as it is found by subtraction. The range given in Table VIII is obtained by assuming level schemes with minimal and maximal feeding of the ground state, constrained by the observed intensities and the neutron separation energy at 1.58(16) MeV [32]. Regardless, the cross section to the lowest $7/2^-$ is only slightly higher than that in ^{38}Si, in agreement with the shell model predictions, and indicating that significant neutron strength lies in orbits above the $f_{7/2}$.

All of the cross section calculations presented use the Hartree-Fock constrained well-depth prescription as detailed in Section III and Ref. [30]. We note that well-depth prescriptions, in general, have come under scrutiny where nucleon transfer involves orbits above the Fermi surface [40], such as the neutron $1p_{3/2}$ state in the case of these neutron-rich silicon isotopes. It was discussed that, for such orbits, the well-depth prescription tends to pull the wave function to smaller radii, producing an orbital wave function whose rms radius is too small. If this is the case, the calculated cross sections, for e.g. $1p_{3/2}$ configurations, using the present procedure [30] will be underestimated. Very small shell model spectroscopic factors (and small experimental cross sections) for neutron knockout from the $1p_{1/2}$ and $0f_{5/2}$ orbits suggests that uncertainty in the single-particle cross section for these orbits should have a negligible impact on the calculated inclusive cross sections in Figure 18. The spectroscopic factors for knockout from the $1p_{3/2}$ orbit are slightly larger, and a very large uncertainty in the single-particle cross section for this orbit could potentially have

an impact on the inclusive cross sections.

As an estimation of the theoretical uncertainty due to the well-depth prescription, we adopt an alternative prescription in which we adjust the radius parameter of the Hartree-Fock constrained Woods-Saxon potential (as opposed to its depth) in order to reproduce the experimental separation energy. The single-particle cross section for removal of a $1p_{3/2}$ neutron increases by 25%, 19%, and 12% – relative to the well-depth prescription – for ^{36}Si, ^{38}Si, and ^{40}Si, respectively. This corresponds to an uncertainty of $\lesssim$ 0.6, 1.5, and 2.7 mb in the theoretical inclusive cross section for the three projectiles, corresponding to 0.7%, 1.5%, and 2.3%. We therefore conclude that this source of uncertainty has minimal impact on the inclusive cross sections shown in Figure 18, and for the exclusive cross sections in Figures 22-24 the impact is probably smaller than the uncertainty from the shell model spectroscopic factors.

VI. LOW-MOMENTUM TAILS

As was discussed in Section III, the residue parallel momentum distributions calculated with the (approximate) eikonal model dynamics are symmetric. By contrast, experimental distributions, including in this work, can display a varying degree of asymmetry depending on the nucleon separation energy, the beam energy, and the experimental acceptances (examples can be found in [41–44]). In the case of light halo systems, Tostevin *et al.* [45] were able to reproduce the observed asymmetry, seen as a low momentum tail to the momentum distribution, by using a continuum-discretized coupled-channels (CDCC) calculation of the elastic breakup mechanism with its exact (energy and momentum conserving) treatment of the target, residue, and removed nucleon three-body dynamics.

The knockout cross section is typically divided into two mechanisms: a diffraction-dissociation reaction in which the target remains in the ground state, and a stripping reaction in which the target is inelastically excited. In light halo-like systems, diffraction is more prevalent and the contributions of the two mechanisms are comparable, while the stripping mechanism dominates transitions that remove more well-bound nucleons, as in the cases studied here. There is no readily applicable, fully-dynamical model of the stripping mechanism and its spectrum of continuum (many-body) target excited states. The closure approximation over this complete set of target excitations and the adiabatic (sudden) approximation used in the eikonal model are very effective for calculating the target-final-state-inclusive knockout reaction probabilities and cross sections, but they approximate the kinematics and energy sharing between the reacting constituents. The result is that energy dissipated in exciting the target is not reflected in the eikonal model residue momentum distributions and, in reality, momentum distributions for reactions with significant target excitation (stripping) cross sections are expected to show low momentum tails.

We note that the transfer to the continuum (TC) model [46] of nucleon removal, which includes dynamical effects beyond the adiabatic approximation, was recently used by Flavigny *et al.* [47] to discuss an extreme asymmetry and distortion of the momentum distribution observed when the removed nucleon was very strongly-bound and the incident beam energy was low – the consequence of a dynamical cut-off on the maximum momentum of the forward going residue due to four-momentum conservation. This kinematical limit [47] does not play any significant role for the beam energies used here. Unfortunately, the geometrical limitations inherent in the formulation of the TC model (discussed e.g. in [48, 49]), which takes only the asymptotic form for the (neutral) removed-particle wave function, is realistic only at peripheral impact parameters and for neutron halo-like systems. The TC model is not applicable for proton removal or for the neutron separation energies, $S_n \gtrsim 5$ MeV, of the current work. There is, as yet, no theoretical model that allows a quantitative prediction of the low momentum behavior of the knockout residue momentum distribution due to target excitation energy (dissipation) effects, for the systems of interest here.

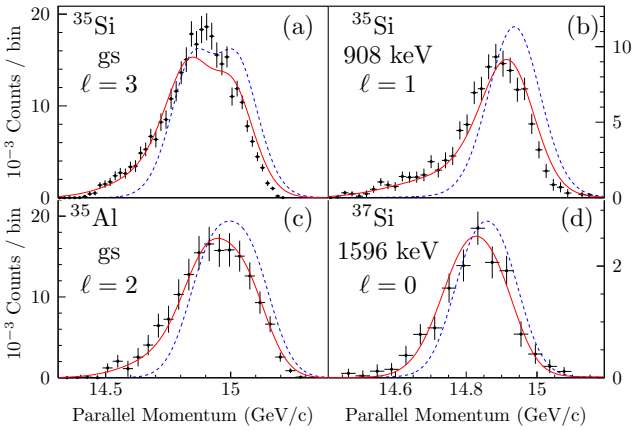

FIG. 25. (Color online) Experimental parallel momentum distributions for the indicated final states of selected knockout residues. The (symmetric) eikonal momentum distributions after folding with (i) the incoming momentum distribution (dashed blue lines) and (ii) the inelastic scattering momentum distribution (solid red lines), as described in the text, are shown, all scaled to the total number of measured counts.

The momentum distribution of Figure 25(b) shows an example of such a tail observed in the neutron knockout reaction from ^{36}Si. We discuss an empirical method to describe this degree of experimentally-observed asymmetry by using a measurement of inelastically-scattered projectiles to approximate the momentum profile of the outgoing residue from the knockout reaction. Figure 26(a) shows the longitudinal momentum distribution of the

outgoing ^{36}Si. [1] The distribution of events consists of a large peak of higher-energy unreacted ions and a smaller tail distribution extending to momenta 0.5 GeV/c (200 MeV of kinetic energy) below the maximum. Figure 26(b) shows the γ-ray spectra gated on these two regions, in units of γ-rays per ion. It is clear that the (blue) unreacted peak is in coincidence only with low-energy atomic background [51], while the production of higher energy γ rays (red) is dominated by events in the tail of the distribution.

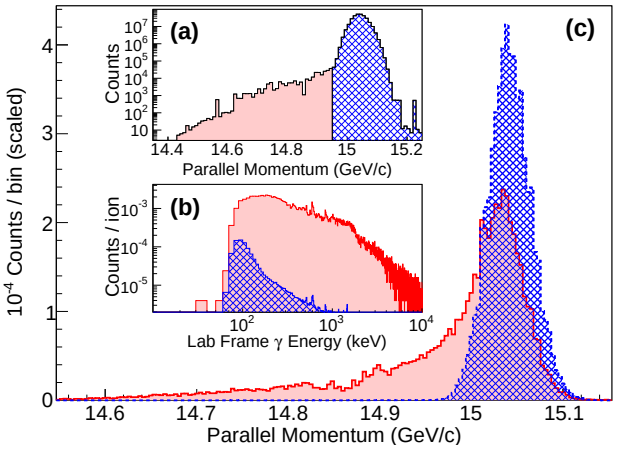

FIG. 26. (Color online) (a) The number of ^{36}Si ions detected in the S800 after impinging the ^{36}Si secondary beam on a beryllium target, as a function of their longitudinal momenta. (b) Gamma rays detected in coincidence with the outgoing ^{36}Si fragments, gated on low-momentum (red filled) and high-momentum (blue hatches) regions of the distribution of panel (a). (c) The unreacted momentum distribution (no γ rays detected) is shown in blue hatches and the momentum distribution in coincidence with a γ-ray with $E_\gamma > 1$ MeV (scaled for comparison) is shown by the solid red filled area.

Such high energy γ-ray background is universally observed in intermediate-energy knockout, inelastic scattering, and Coulomb excitation reactions, while it is absent in the more-exclusive fast nucleon-pickup reactions [50]. The origin of this background is most probably the interactions of target breakup products (neutron and charged particles) with the aluminum beam pipe, as evidenced by their delayed timing [52], and anti-correlation with the trajectory of the outgoing fragment in the azimuthal direction.

This γ-ray background may then serve as a tag on events in which the target nucleus was excited (^{9}Be has no bound excited states). The additional requirement that the heavy projectile survives the collision selects events similar to those involved in the surface-localized single-nucleon knockout reactions. Figure 26(c) shows the parallel momentum distribution, derived from panel (a), with gates for no γ rays (blue), or for events with γ-ray energy $E_\gamma > 1$ MeV (red). [2] The former distribution is narrow and symmetric, reflecting the momentum distribution of the incoming ^{36}Si beam. In contrast, the distribution gated on energetic γ rays is asymmetric, with a substantial low-momentum tail. Changing the γ-ray energy cut – e.g. taking all events above 500 keV – has little effect on the resulting momentum distribution. It is reasonable to expect that this asymmetric distribution approximates the corresponding dissipative processes present in the one-nucleon knockout reactions.

Figure 25 shows the results of such an analysis for four typical knockout reaction transitions. The blue dashed curves are obtained when the symmetric, projectile rest frame, eikonal model momentum distributions are Lorentz boosted to the laboratory frame and folded with the incoming beam momentum distribution, a standard procedure. The solid red curves result when the Lorentz boosted shapes of the eikonal distributions are folded instead with the empirical, projectile-dependent and asymmetric distribution $\mathcal{F}(p)$, derived from inelastic scattering. In the case of the ^{36}Si-induced reactions, this is derived from (and is similar to) the red distribution presented in Figure 26(c), but with due consideration of the change in mass and the different energy straggling through the target of the knockout residues. These corrections are discussed in an appendix. As shown in Figure 25, this procedure leads to a better description of the experimental momentum distributions and reproduces well the degree of asymmetry seen in the measurements. This agreement suggests that the perturbed shapes of the observed knockout reaction residue momentum distributions, attributed to dissipative (target excitation) processes, can be modeled by application of an empirical correction, deduced from projectile inelastic scattering events, to the calculated eikonal model distributions. This procedure has been used consistently in the comparisons between the measured and calculated momentum distributions throughout this paper. A fully-theoretical description of these dissipative processes remains as a challenge for future work.

VII. SUMMARY

Intermediate energy one-proton and one-neutron knockout reactions were used to probe the evolution of single-particle structure in neutron-rich silicon isotopes between N=20 and N=28. We show that the Z=14 sub-shell closure remains relatively good up to ^{40}Si,

[1] The trigger condition used while taking these data recorded all particle-γ coincidences, and every 200th particle event, even if it came without an accompanying γ ray. The distributions in Figure 26 have been corrected accordingly.

[2] Due to the finite γ-ray detection efficiency, some events which produce a γ-ray will of course be included in the no-γ spectrum. However, the number of these events are negligible compared to true no-γ events.

while there are substantial neutron excitations across the N=28 gap. The one-proton knockout reactions enabled the first spectroscopy of excited states in ^{35,37,39}Al, and one-neutron knockout enabled spin and parity assignments for several low-lying states in ^{35,37,39}Si. We have observed a γ decay of a state in ^{35}Si which is unbound to neutron emission by over 1 MeV, produced with a small cross section. Both structural and multi-step reaction mechanism paths to this observation are discussed, including an estimate of the production cross section of a plausible two-step process. We have also used analysis of inelastic scattering events to estimate the effect of inelastic target excitations on the shape of the momentum distribution of the knockout reaction residue. A good description of the asymmetry in the measured momentum distributions was obtained. In general, a good agreement is found between the measured data and the shell model predictions, lending support to the microscopic interpretation of the evolving shell structure near ^{42}Si.

ACKNOWLEDGMENTS

We thank the staff of the Coupled Cyclotron Facility for the delivery of high-quality beams, and Professor L. Riley for the developing and providing the GRETINA simulation code. S.R.S. would also like to thank Professors F. Nunes and C. Bertulani for helpful discussions of reaction theory, and J. K. Smith for discussions concerning neutron-unbound states. This material is based upon work supported by the Department of Energy National Nuclear Security Administration under Award Number DE-NA0000979. This work was also supported by the National Science Foundation under Grant No. PHY-1068217. GRETINA was funded by the US DOE - Office of Science. Operation of the array at NSCL is supported by NSF under Cooperative Agreement PHY-1102511(NSCL) and DOE under grant DE-AC02-05CH11231(LBNL). J.A.T. acknowledges support of the Science and Technology Facilities Council (UK) grant ST/J000051.

Appendix A: Estimate of the two-step knockout cross section

To estimate the yield from a higher-order removal mechanism, we assume a two-step reaction in which the incident ^{36}Si is first excited to its first 2^+ state, and a neutron is then removed. Such a process is plausible given the (overlapping) surface localization of the two reaction mechanisms. The joint probability for this two-step reaction as a function of the projectile's impact parameter, b, is computed from the deduced impact parameter dependences of the cross sections (reaction probabilities) $\mathrm{d}\sigma/\mathrm{d}b$, for the $0^+ \rightarrow 2^+$ inelastic excitation and the neutron removal from the 2^+_1 state. The former is deduced from a conventional inelastic scattering calculation made using the direct reactions code FRESCO [54] and the latter is extracted from the eikonal model calculation of the single-particle cross section. The resulting joint probability, integrated over impact parameters, is then multiplied by the SDPF-MU shell-model spectroscopic factor for knockout to the candidate 3611 keV final states of ^{35}Si. Essentially identical results are obtained if, instead, one assumes the probability of projectile excitation to the 2^+_1 state to be the ratio of the total inelastic and elastic cross sections, with the latter computed from the eikonal model S-matrix for ^{36}Si + ^{9}Be scattering using the methodology discussed in Section III.

Appendix B: Corrections to the measured inelastic momentum distribution

We denote the measured inelastic momentum distribution in coincidence with high-energy γ-rays $F_{inel}(p)$, where p is in the lab frame. In the knockout reaction, momentum per nucleon is approximately conserved, so this distribution is scaled by $(A-1)/A$. For the measurements of ^{36}Si and ^{38}Si, a different target thickness was used for the knockout and inelastic scattering experiments. The extra energy loss in the thicker target was estimated by the difference in centroid momenta between the inelastic scattering run (with no gate on γ-rays) and the unreacted beam particles in the knockout setting:

$$\Delta_{tgt} = \langle P \rangle_{unreacted} - \langle P \rangle_{inel} \,. \tag{B1}$$

Further, the mass A and mass $(A-1)$ systems have different energy loss through the target, particularly for proton knockout. This difference in outgoing momentum is estimated by the parameter δp, which is the difference in outgoing momenta after the full target thickness for the mass A and mass $A-1$ systems, estimated with the program LISE++ [53]. The reaction takes place at any depth in the target with approximately equal probability, so the effect of the different energy loss is handled with two Heaviside functions

$$h(p, \delta p) = |\Theta(p - \delta p) - \Theta(p)| \,. \tag{B2}$$

We therefore obtain a corrected inelastic distribution

$$\mathcal{F}(p) = F_{inel}\left(\frac{A}{A-1}p - \Delta_{tgt}\right) * h(p, \delta p) \tag{B3}$$

where $*$ indicates a convolution. The distribution $\mathcal{F}(p)$ accounts for all effects other than the recoil of the removed nucleon.

The recoil is handled by the eikonal calculation, which produces a distribution $G_{eik}(p_{cm})$ in the projectile rest frame. The final theoretical curve $\mathcal{K}(p)$ which corresponds to the red curves in Figure 25 is obtained by

$$\mathcal{K}(p) = \mathcal{F}(p) * G_{eik}(p/\gamma) \tag{B4}$$

where the relativistic factor γ in the eikonal distribution accounts for the broadening due to the Lorentz boost to

the lab frame. The blue curves in Figure 25 are obtained by replacing the inelastic scattering distribution with the unreacted distribution $F_{inel}(p) \rightarrow F_{unreacted}(p)$ in (B3) and by taking $\Delta_{tgt} = 0$.

[1] J. D. Holt, T. Otsuka, A. Schwenk and T. Suzuki, J. Phys. G 39 085111 (2012)
[2] T. Glasmacher *et al.*, Phys. Lett. B 395, 163 (1997)
[3] P. D. Cottle and K. W. Kemper, Phys. Rev. C 58, 3761 (1998)
[4] B. Bastin *et al.*, Phys. Rev. Lett. 99, 022503 (2007)
[5] S. Takeuchi *et al.*, Phys. Rev. Lett. 109, 182501 (2012)
[6] L. Gaudefroy *et al.*, Phys. Rev. Lett. 97, 092501 (2006)
[7] Y. Utsuno, T. Otsuka, B. A. Brown, M. Honma, T. Mizusaki, and N. Shimizu, Phys. Rev. C 86 051301(R) (2012)
[8] T. Otsuka, T. Suzuki, R. Fujimoto, H. Grawe, and Y. Akaishi, Phys. Rev. Lett. 95, 232502 (2005).
[9] A. Gade *et al.*, Phys. Rev. C 74, 034322 (2006)
[10] G. Burgunder *et al.*, Phys. Rev. Lett. 112, 042502 (2014)
[11] A. P. Zuker, J. Retamosa, A. Poves, and E. Caurier, Phys. Rev. C 52 R1741 (1995)
[12] T. Otsuka, T. Suzuki, M. Honma, Y. Utsuno, N. Tsunoda, K. Tsukiyama, and M. Hjorth-Jensen, Phys. Rev. Lett. 104, 012501 (2010)
[13] D. J. Morrissey, B. M. Sherrill, M. Steiner, A. Stolz, and I. Wiedenhoever, Nucl. Instrum. Methods in Phys. Res. B 204, 90 (2003).
[14] D. Bazin, J. A. Caggiano, B. M. Sherrill, J. Yurkon, and A. Zeller, Nucl. Instrum. Methods in Phys. Res. B 204, 629 (2003).
[15] M. Berz, K. Joh, J. A. Nolen, B. M. Sherrill and A. F. Zeller, Phys. Rev. C. 47, 537 (1993)
[16] S. Paschalis *et al.*, Nucl. Instr. Meth. Phys. Res. A 79, 44 (2013)
[17] S. Agostinelli *et al.* (Geant4 Collaboration), Nucl. Instr. Methods in Phys. Res. A 506, 250 (2003)
[18] E. Farnea, F. Recchia, D. Bazzacco, Th. Kröll, Zs. Podolyák, B. Quintana, A. Gadea, and The AGATA Collaboration, Nucl. Instrum. Methods in Phys. Res. B 621, 331 (2010).
[19] S. R. Stroberg Ph.D. Thesis, Michigan State University (2014)
[20] NuShellX@MSU, B. A. Brown, W. D. M. Rae, E. McDonald, and M. Horoi, `http://www.nscl.msu.edu/~brown/resources/resources.html`; NuShellX, W. D. M. Rae, `http://www.garsington.eclipse.co.uk/`.
[21] F. Nowacki and A. Poves, Phys. Rev. C 79, 014310 (2009).
[22] S. Nummela *et al.*, Phys. Rev. C 63, 044316 (2001)
[23] K. Steiger, Ph.D. Thesis, TU München (Germany) (2013)
[24] D. H. Gloeckner and R. D. Lawson, Phys. Lett. B 53, 313 (1974)
[25] M. De Rydt *et al.*, Phys. Rev. C 81, 034308 (2010)
[26] P. G. Hansen and J. A. Tostevin, Annu. Rev. Nucl. Part. Sci 53, 219 (2003)
[27] A. E. L. Dieperink and T. L. de Forest, Jr., Phys. Rev. C 10, 2 (1974)
[28] B. A. Brown, Phys. Rev. C. 58, 220 (1998)
[29] S. C. Pieper, K. Varga, and R. B. Wiringa, Phys. Rev. C. 66 044310 (2002)
[30] A. Gade, *et al.*, Phys. Rev. C 77, 044306 (2008)
[31] C. A. Bertulani and A. Gade, Comp. Phys. Comm. 175, 372 (2006)
[32] M. Wang, G. Audi, A. H. Wapstra, F. G. Kondev, M. MacCormick, X. Xu, and B. Pfeiffer, Chinese Physics C 36 1603 (2012)
[33] A. Gade *et al.*, Phys. Lett. B 666 218 (2008)
[34] F. Rotaru *et al.*, Phys. Rev. Lett. 109, 092503 (2012)
[35] R. W. Ibbotson, T. Glasmacher, P. F. Mantica, and H. Scheit, Phys. Rev. C 59, 642 (1999)
[36] R. W. Ibbotson *et al.* Phys. Rev. Lett. 80, 2081 (1998)
[37] X. Liang *et al.* Phys. Rev. C 74, 014311 (2006)
[38] D. Sohler *et al.*, Phys. Lett. B. 703, 417 (2011)
[39] J. Enders *et al.*, Phys. Rev. C. 65, 034318 (2002)
[40] R. J. Philpott and W. T. Pinkston, Nucl. Phys. A 119, 241 (1968)
[41] A. Navin, *et al.*, Phys. Rev. Lett. 81, 5089 (1998)
[42] A. Gade, *et al.*, Phys. Rev. C 71, 051301(R) (2005)
[43] K. L. Yurkewicz, *et al.* Phys. Rev. C 74 024304 (2006)
[44] L. A. Riley, *et al.*, Phys. Rev. C 86, 047301 (2012)
[45] J. A. Tostevin, D. Bazin, B. A. Brown, T. Glasmacher, P. G. Hansen, V. Maddalena, A. Navin, and B. M. Sherrill, Phys. Rev. C. 66 024607 (2002)
[46] A. Bonaccorso and D. M. Brink, Phys. Rev. C 38, 1776 (1988)
[47] F. Flavigny, A. Obertelli, A. Bonaccorso, G. F. Grinyer, C. Louchart, L. Nalpas, and A. Signoracci, Phys. Rev. Lett 108, 252501 (2012)
[48] A. Bonaccorso and G. F. Bertsch, Phys. Rev. C 63, 044604 (2001).
[49] A. García-Camacho, R. C. Johnson and J. A. Tostevin, Phys. Rev. C 71, 044606 (2005).
[50] A. Gade, *et al.*, Phys. Rev. C 76, 061302(R) (2007).
[51] Zs. Podolyák, *et al.* Nucl. Phys. A 722, 273c (2003).
[52] D. Weisshaar, *et al.* Nucl. Instr. Methods in Phys. Res. A 594, 56 (2008).
[53] O. Tarasov and D. Bazin, Nucl. Instr. Methods in Phys. Res. B 266, 4657 (2008).
[54] I. J. Thompson, Comput. Phys. Rep. 7, 167 (1988)